Supporting Information for

Oceanic enrichment of ammonium and its impacts on phytoplankton community composition under a high-emissions scenario

Pearse J. Buchanan[1,2,3], Juan J. Pierella Karlusich[4,5], Robyn E. Tuerena[6], Roxana Shafiee[7], E. Malcolm S. Woodward[8], Chris Bowler[9,10], and Alessandro Tagliabue[2].

[1]CSIRO Environment, Hobart, 7004, Australia.

[2]Department of Earth, Ocean and Ecological Sciences, University of Liverpool; Liverpool, L69 3GP, UK.

[3]Department of Global Ecology, Carnegie Institution for Science; Stanford, CA, 94305, USA.

[4]FAS Division of Science, Harvard University, Cambridge, MA, 02138, USA.

[5]Department of Biology, Massachusetts Institute of Technology, Cambridge, MA, 02139, USA.

[6]Scottish Association for Marine Science; Dunstaffnage, Oban, PA37 1QA, UK.

[7]Center for the Environment, Harvard University, Cambridge, MA, 02138.

[8]Plymouth Marine Laboratory; Plymouth, PL1 3DH, UK.

[9]Institut de Biologie de l'École Normale Supérieure, Département de Biologie, École Normale Supérieure, CNRS, INSERM, Université de Recherche Paris Sciences et Lettres, Paris, France.

[10]CNRS Research Federation for the study of Global Ocean Systems Ecology and Evolution, FR2022/Tara Oceans GEOSEE, Paris, France.

Contents of this file

Text S1 to S2
Figures S1 to S17
Tables S1 to S3

Additional Supporting Information (Files uploaded separately)

Data Sets S1 to S4

Introduction

In Text S1 we provide additional information on how ammonia oxidation and nitrite oxidation is computed within the ocean biogeochemical model. In Text S2 we evaluate the ocean biogeochemical model against observational nutrient and rate datasets (provided in Data S1-S4). Figures S1-S20 and Tables S1-S3 are provided to support the conclusions of the main text.

Text S1.

Nitrification in PISCES-v2 was previously treated as a one-step conversion of NH_4^+ to NO_3^- but was split into its two component steps (ammonia and nitrite oxidation) for the purposes of this study. Both steps were simulated implicitly by multiplying a maximum growth rate μ^{max} (day^{-1}) by the concentration of substrate (μM) to return a maximum potential rate (μM day^{-1}). This was then multiplied by limitation terms (L^X) representing the effect of environmental conditions to return the realized rate.

For ammonia oxidation ($[NH_4^+] \rightarrow [NO_2^-]$),

$$[NH_4^+] \rightarrow [NO_2^-] = \mu_{AO}^{max} \cdot [NH_4^+] \cdot L_{AO}^{NH_4^+} \cdot L_{AO}^{PAR} \cdot L_{AO}^{pH} \quad (1)$$

$$\mu_{AO}^{max} = \max(0.2, 0.029 \cdot T - 0.147) \quad (2)$$

$$L_{AO}^{NH_4^+} = \frac{NH_4^+}{NH_4^+ + K_{AO}^{NH_4^+}} \quad (3)$$

$$L_{AO}^{PAR} = 1 - \frac{PAR}{PAR + K_{AO}^{PAR}} \quad (4)$$

$$L_{AO}^{pH} = \min\left(1, \frac{10^{(pH - pK_a)}}{10^{(R_{pH} - pK_a)}}\right) \quad (5)$$

In the above, μ_{AO}^{max} is estimated by a linear model with a floor of 0.2 day^{-1} (Eqn. 2). This model was fit to the growth curves of three ecotypes of ammonia-oxidizing archaea (Qin et al., 2015) and returns rates of 0.8 day^{-1} near 30°C (Fig. S17). A floor of 0.2 day^{-1} was justified by relatively high rates observed in near-freezing waters (Tolar et al., 2016). The limitation term for NH_4^+ uptake ($L_{AO}^{NH_4^+}$, Eqn. 3) assumes a constant half-saturation

coefficient $K_{AO}^{NH_4^+}$ of 0.1 μM, which is well reflective of both natural marine assemblages of archaea (Horak et al., 2013; Newell et al., 2013; Olson, 1981; Peng et al., 2016; Wan et al., 2018) and the cultivated archaea *Nitrosopumilus maritimus* SCM1 (Martens-Habbena et al., 2009). Light limitation (L_{AO}^{PAR}) and effects of pH (L_{AO}^{pH}) are less well constrained, but nonetheless important. We set the half saturation term of photoinhibition (K_{AO}^{PAR}, Eqn. 4) to 0.75 W m^{-2}, which accounted for an 80% reduction in rates at photosynthetically active radiation levels of 3 W m^{-2} (Merbt et al., 2012). We set the reference pH (R_{pH}, Eqn. 5) below which negative effects on oxidation occur at 8.0, which reflects surface conditions of historical ocean and therefore the pH (i.e., NH_3 availability) that ammonia oxidizers are likely adapted to (Ward, 1987). With a pK_a of the NH_3-NH_4^+ equilibrium equal to 9.3 (Zeebe and Wolf-Gladrow, 2001), this treatment reduced oxidation rates by 27.5% for a decline in pH of 0.14 units, which is a more conservative change than the 36-38% declines in oxidation reported by Beman et al. (2011) for the same pH change.

For nitrite oxidation ($[NO_2^-] \rightarrow [NO_3^-]$),

$$[NO_2^-] \rightarrow [NO_2^-] = \mu_{NO}^{max} \cdot [NO_2^-] \cdot L_{NO}^{NO_2^-} \cdot L_{NO}^{PAR} \quad 6$$

$$L_{NO}^{NO_2^-} = \frac{NO_2^-}{NO_2^- + K_{NO}^{NO_2^-}} \quad 7$$

$$L_{NO}^{PAR} = 1 - \frac{PAR}{PAR + K_{AO}^{PAR}} \quad 8$$

The treatment of nitrite oxidation is like ammonia oxidation. However, there are two key differences. First, nitrite-oxidizing bacteria have lower growth yield per unit nitrogen oxidized compared to ammonia-oxidizing archaea (Bayer et al., 2022), which demands a slower growth rate in our model given that we are simulating this metabolism implicitly. Accordingly, we set the maximum growth rate of nitrite-oxidizing bacteria (μ_{NO}^{max}) to a constant 0.15 day^{-1}, informed by doubling times in excess of four days of marine cultures held at optimal conditions (Spieck and Lipski, 2011). Second, pH has no effect on NO_2^- concentrations. Otherwise, we maintain the same half-saturation coefficients for the substrate ($L_{NO}^{NO_2^-}$, Eqn. 7) and light limitation (L_{NO}^{PAR}, Eqn. 8) terms as for ammonia

oxidizers, being 0.1 μM for $K_{NO}^{NO_2^-}$ and 0.75 W m^{-2} for K_{NO}^{PAR} (Table S3). All parameters for nitrification are presented in Table S3.

We did not include oxygen or iron limitation. Oxygen was ignored due to reports of high activity and biomass of nitrifiers in low oxygen zones, due perhaps to a combination of high cellular affinity for oxygen (Bristow et al., 2016) and potential anaerobic pathways of oxidation via alternative electron acceptors (Babbin et al., 2020; Kraft et al., 2022). We ignored iron limitation, despite its potential for limiting growth of ammonia oxidizers (Shafiee et al., 2019), because little is known regarding its effects on the growth of nitrite-oxidizing bacteria. In addition, changes to the availability of iron for biology in the future ocean are highly uncertain and models have little skill in this regard (Tagliabue et al., 2016). We acknowledge, however, that changes in both oxygen and iron availability may be important additional factors governing shifts in the NH_4^+ to DIN ratio in a future ocean.

Text S2.

Concentrations of 0.1 μM NH_4^+ or greater exist over continental shelves and in regions of strong mixing with high rates of primary production and subsequent heterotrophy. This accumulation of NH_4^+ in productive regions is reproduced by our model (Fig. S1a). However, as high NH_4^+ co-occurs with high NO_3^- concentrations, NH_4^+ makes a small contribution to total DIN in these upwelling systems (Fig. S1b), which include the eastern tropical Pacific, eastern boundary upwelling systems, the northwest Indian Ocean, the subpolar gyres and the Southern Ocean (although we note that the model underestimates NH_4^+ concentrations in the Southern Ocean). In contrast, low NH_4^+ concentrations of less than 0.05 μM pervade the oligotrophic gyres of the lower latitudes. As these regions also display very low NO_3^- concentrations, NH_4^+ makes up a much higher fraction of total DIN in both the observations and our model, with the NH_4^+ peak occurring deeper in the water column (Fig. S2).

Eutrophic upwelling systems and oligotrophic waters differed in the major sinks of NH_4^+ (Fig. S1c), consistent with available observations and constraints from theory. In eutrophic waters (defined by surface nitrate > 1 μM), ammonia oxidation represented 49

± 29 % (mean ± standard deviation) of NH_4^+ sinks, but this dropped to 32 ± 9 % in oligotrophic systems. Measured rates of ammonia oxidation showed a positive relationship with surface NO_3^- concentrations and this was reproduced by the model (Fig. S3), indicating that ammonia oxidation was indeed a greater proportion of the overall NH_4^+ budget in eutrophic regions. In agreement, isotopic methods have shown that the bulk of nitrogen assimilated by phytoplankton in oligotrophic waters is recycled (Eppley and Peterson, 1979; Fawcett et al., 2011; Klawonn et al., 2019; Van Oostende et al., 2017; Wan et al., 2021), implying that most nitrogen cycling occurs without ammonia oxidation. Again, our model reproduces this feature of oligotrophic systems (Fig. S1c).

Supplementary References

1. Babbin, A. R., Buchwald, C., Morel, F. M. M., Wankel, S. D., and Ward, B. B.: Nitrite oxidation exceeds reduction and fixed nitrogen loss in anoxic Pacific waters, Mar Chem, 224, 103814, https://doi.org/10.1016/j.marchem.2020.103814, 2020.
2. Bayer, B., McBeain, K., Carlson, C. A., and Santoro, A. E.: Carbon content, carbon fixation yield and dissolved organic carbon release from diverse marine nitrifiers, Limnol Oceanogr, https://doi.org/10.1002/lno.12252, 2022.
3. Beman, J. M., Chow, C. E., King, A. L., Feng, Y., Fuhrman, J. A., Andersson, A., Bates, N. R., Popp, B. N., and Hutchins, D. A.: Global declines in oceanic nitrification rates as a consequence of ocean acidification, Proc Natl Acad Sci U S A, 108, 208–213, https://doi.org/10.1073/pnas.1011053108, 2011.
4. Bristow, L. A., Dalsgaard, T., Tiano, L., Mills, D. B., Bertagnolli, A. D., Wright, J. J., Hallam, S. J., Ulloa, O., Canfield, D. E., Revsbech, N. P., and Thamdrup, B.: Ammonium and nitrite oxidation at nanomolar oxygen concentrations in oxygen minimum zone waters, Proceedings of the National Academy of Sciences, 113, 10601–10606, https://doi.org/10.1073/pnas.1600359113, 2016.
5. Eppley, R. W. and Peterson, B. J.: Particulate organic matter flux and planktonic new production in the deep ocean, Nature, 282, 677–680, https://doi.org/10.1038/282677a0, 1979.
6. Fawcett, S. E., Lomas, M. W., Casey, J. R., Ward, B. B., and Sigman, D. M.: Assimilation of upwelled nitrate by small eukaryotes in the Sargasso Sea, Nat Geosci, 4, 717–722, https://doi.org/10.1038/ngeo1265, 2011.
7. Follows, M. J., Dutkiewicz, S., Grant, S., and Chisholm, S. W.: Emergent Biogeography of Microbial Communities in a Model Ocean, Science (1979), 315, 1843–1846, https://doi.org/10.1126/science.1138544, 2007.
8. Garcia, H. E., Weathers, K. W., Paver, C. R., Smolyar, I., Boyer, T. P., Locarnini, R. A., Zweng, M. M., Mishonov, A. V., Baranova, O. K., Seidov, D., and Reagan, J. R.: World Ocean Atlas 2018. Volume 4 : Dissolved Inorganic Nutrients (phosphate, nitrate and nitrate+nitrite, silicate)., edited by: Editor, A. M. T., 35 pp., 2019.
9. Horak, R. E. A., Qin, W., Schauer, A. J., Armbrust, E. V., Ingalls, A. E., Moffett, J. W., Stahl, D. A., and Devol, A. H.: Ammonia oxidation kinetics and temperature sensitivity of a natural marine community dominated by Archaea, ISME J, 7, 2023–2033, https://doi.org/10.1038/ismej.2013.75, 2013.
10. Klawonn, I., Bonaglia, S., Whitehouse, M. J., Littmann, S., Tienken, D., Kuypers, M. M. M., Brüchert, V., and Ploug, H.: Untangling hidden nutrient dynamics: rapid ammonium cycling and single-cell ammonium assimilation in marine plankton communities, ISME J, 13, 1960–1974, https://doi.org/10.1038/s41396-019-0386-z, 2019.

11. Kraft, B., Jehmlich, N., Larsen, M., Bristow, L. A., Könneke, M., Thamdrup, B., and Canfield, D. E.: Oxygen and nitrogen production by an ammonia-oxidizing archaeon, Science (1979), 375, 97–100, https://doi.org/10.1126/science.abe6733, 2022.
12. Martens-Habbena, W., Berube, P. M., Urakawa, H., de la Torre, J. R., and Stahl, D. A.: Ammonia oxidation kinetics determine niche separation of nitrifying Archaea and Bacteria, Nature, 461, 976–979, https://doi.org/10.1038/nature08465, 2009.
13. Merbt, S. N., Stahl, D. A., Casamayor, E. O., Martí, E., Nicol, G. W., and Prosser, J. I.: Differential photoinhibition of bacterial and archaeal ammonia oxidation, FEMS Microbiol Lett, 327, 41–46, https://doi.org/10.1111/j.1574-6968.2011.02457.x, 2012.
14. Newell, S. E., Fawcett, S. E., and Ward, B. B.: Depth distribution of ammonia oxidation rates and ammonia-oxidizer community composition in the Sargasso Sea, Limnol Oceanogr, 58, 1491–1500, https://doi.org/10.4319/lo.2013.58.4.1491, 2013.
15. Olson, R. J.: Differential photoinhibition of marine nitrifying bacteria: a possible mechanism for the formation of the primary nitrite maximum, J Mar Res, 39, 227–238, 1981.
16. Van Oostende, N., Fawcett, S. E., Marconi, D., Lueders-Dumont, J., Sabadel, A. J. M., Woodward, E. M. S., Jönsson, B. F., Sigman, D. M., and Ward, B. B.: Variation of summer phytoplankton community composition and its relationship to nitrate and regenerated nitrogen assimilation across the North Atlantic Ocean, Deep Sea Research Part I: Oceanographic Research Papers, 121, 79–94, https://doi.org/10.1016/j.dsr.2016.12.012, 2017.
17. Peng, X., Fuchsman, C. A., Jayakumar, A., Warner, M. J., Devol, A. H., and Ward, B. B.: Revisiting nitrification in the Eastern Tropical South Pacific: A focus on controls, J Geophys Res Oceans, 121, 1667–1684, https://doi.org/10.1002/2015JC011455, 2016.
18. Qin, W., Carlson, L. T., Armbrust, E. V., Devol, A. H., Moffett, J. W., Stahl, D. A., and Ingalls, A. E.: Confounding effects of oxygen and temperature on the TEX 86 signature of marine Thaumarchaeota, Proceedings of the National Academy of Sciences, 112, 10979–10984, https://doi.org/10.1073/pnas.1501568112, 2015.
19. Shafiee, R. T., Snow, J. T., Zhang, Q., and Rickaby, R. E. M.: Iron requirements and uptake strategies of the globally abundant marine ammonia-oxidising archaeon, Nitrosopumilus maritimus SCM1, ISME J, https://doi.org/10.1038/s41396-019-0434-8, 2019.
20. Shiozaki, T., Ijichi, M., Isobe, K., Hashihama, F., Nakamura, K., Ehama, M., Hayashizaki, K., Takahashi, K., Hamasaki, K., and Furuya, K.: Nitrification and its influence on biogeochemical cycles from the equatorial Pacific to the Arctic Ocean, ISME J, 10, 2184–2197, https://doi.org/10.1038/ismej.2016.18, 2016.
21. Spieck, E. and Lipski, A.: Cultivation, Growth Physiology, and Chemotaxonomy of Nitrite-Oxidizing Bacteria, in: Methods in Enzymology, vol. 486, Elsevier Inc., 109–130, https://doi.org/10.1016/B978-0-12-381294-0.00005-5, 2011.
22. Tagliabue, A., Aumont, O., DeAth, R., Dunne, J. P., Dutkiewicz, S., Galbraith, E., Misumi, K., Moore, J. K., Ridgwell, A., Sherman, E., Stock, C., Vichi, M., Völker, C., and Yool, A.: How well do global ocean biogeochemistry models simulate dissolved iron distributions?, Global Biogeochem Cycles, 30, 149–174, https://doi.org/10.1002/2015GB005289, 2016.
23. Tolar, B. B., Ross, M. J., Wallsgrove, N. J., Liu, Q., Aluwihare, L. I., Popp, B. N., and Hollibaugh, J. T.: Contribution of ammonia oxidation to chemoautotrophy in Antarctic coastal waters, ISME J, 10, 2605–2619, https://doi.org/10.1038/ismej.2016.61, 2016.
24. Wan, X. S., Sheng, H.-X., Dai, M., Zhang, Y., Shi, D., Trull, T. W., Zhu, Y., Lomas, M. W., and Kao, S.-J.: Ambient nitrate switches the ammonium consumption pathway in the euphotic ocean, Nat Commun, 9, 915, https://doi.org/10.1038/s41467-018-03363-0, 2018.
25. Wan, X. S., Sheng, H., Dai, M., Church, M. J., Zou, W., Li, X., Hutchins, D. A., Ward, B. B., and Kao, S.: Phytoplankton-Nitrifier Interactions Control the Geographic Distribution of Nitrite in the Upper Ocean, Global Biogeochem Cycles, 35, 1–19, https://doi.org/10.1029/2021GB007072, 2021.
26. Ward, B. B.: Kinetic studies on ammonia and methane oxidation by Nitrosococcus oceanus, Arch Microbiol, 147, 126–133, https://doi.org/10.1007/BF00415273, 1987.
27. Yingling, N., Kelly, T. B., Shropshire, T. A., Landry, M. R., Selph, K. E., Knapp, A. N., Kranz, S. A., and Stukel, M. R.: Taxon-specific phytoplankton growth, nutrient utilization and light limitation in the oligotrophic Gulf of Mexico, J Plankton Res, 1–21, https://doi.org/10.1093/plankt/fbab028, 2021.

28. Zeebe, R. E. and Wolf-Gladrow, D. A.: CO2 in seawater: equilibrium, kinetics, isotopes, 65th ed., Gulf Professional Publishing, 2001.

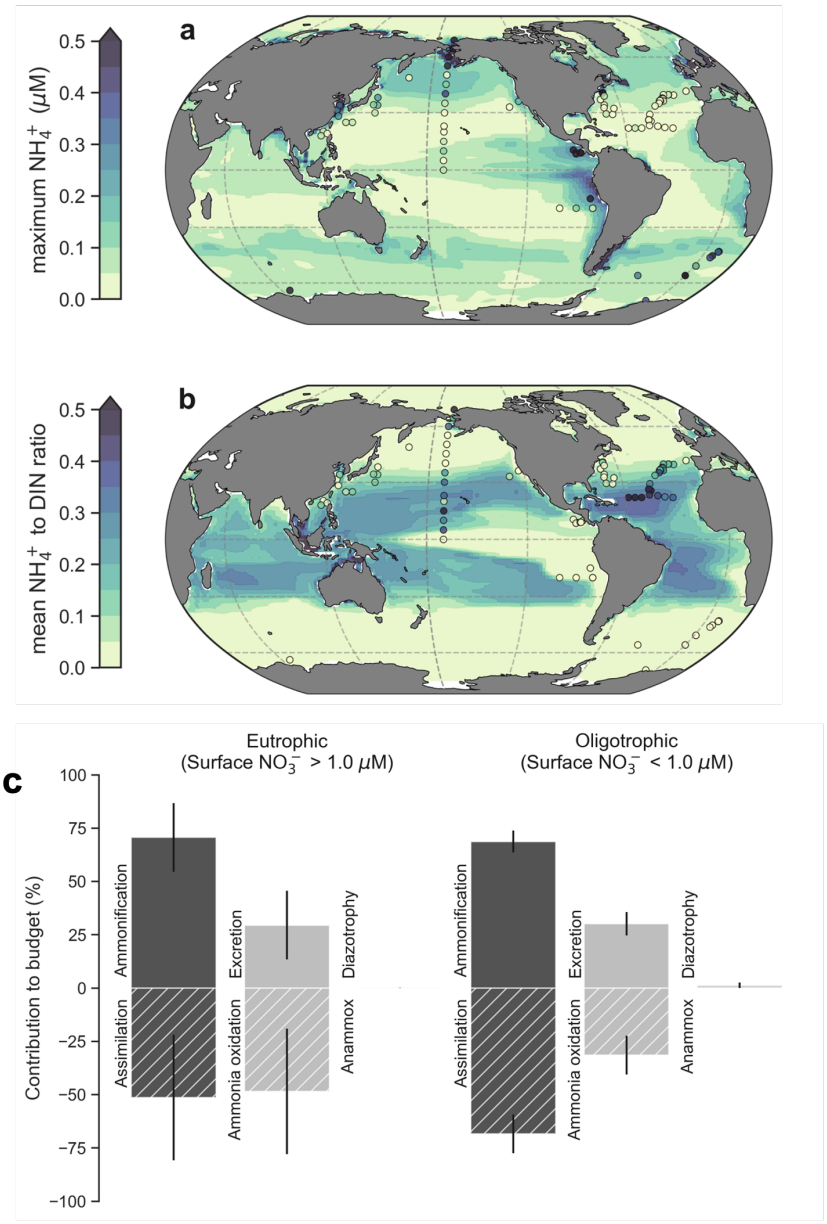

Figure S1. Global patterns of NH_4^+ concentrations, its contribution to DIN in the euphotic zone, and NH_4^+ budgets. (**a**) The simulated maximum NH_4^+ concentration within the euphotic zone. The maximum was chosen to emphasise basin-scale variations. (**b**) Average values of the NH_4^+:DIN ratio. Modelled values are annual averages of the preindustrial control simulation between years 2081-2100. Observed values following linear interpolation between the surface and 200 metres depth are overlaid as coloured markers. Only those profiles with at least 3 data points within the upper 200 metres are shown. (**c**) Global mean ± standard deviations of NH_4^+ fluxes separated into eutrophic and oligotrophic regions. Sources of NH_4^+ are represented by positive values and sinks by negative values.

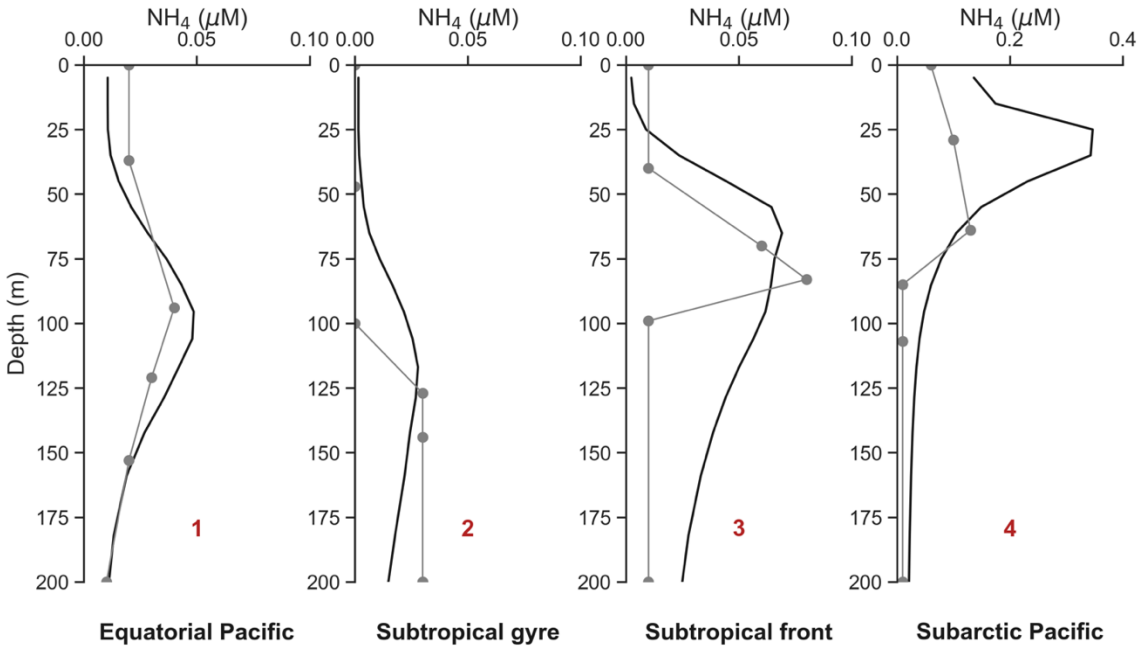

Figure S2. Simulated and observed depth profiles of NH_4^+ at four locations in the North Pacific Ocean (Shiozaki et al., 2016).

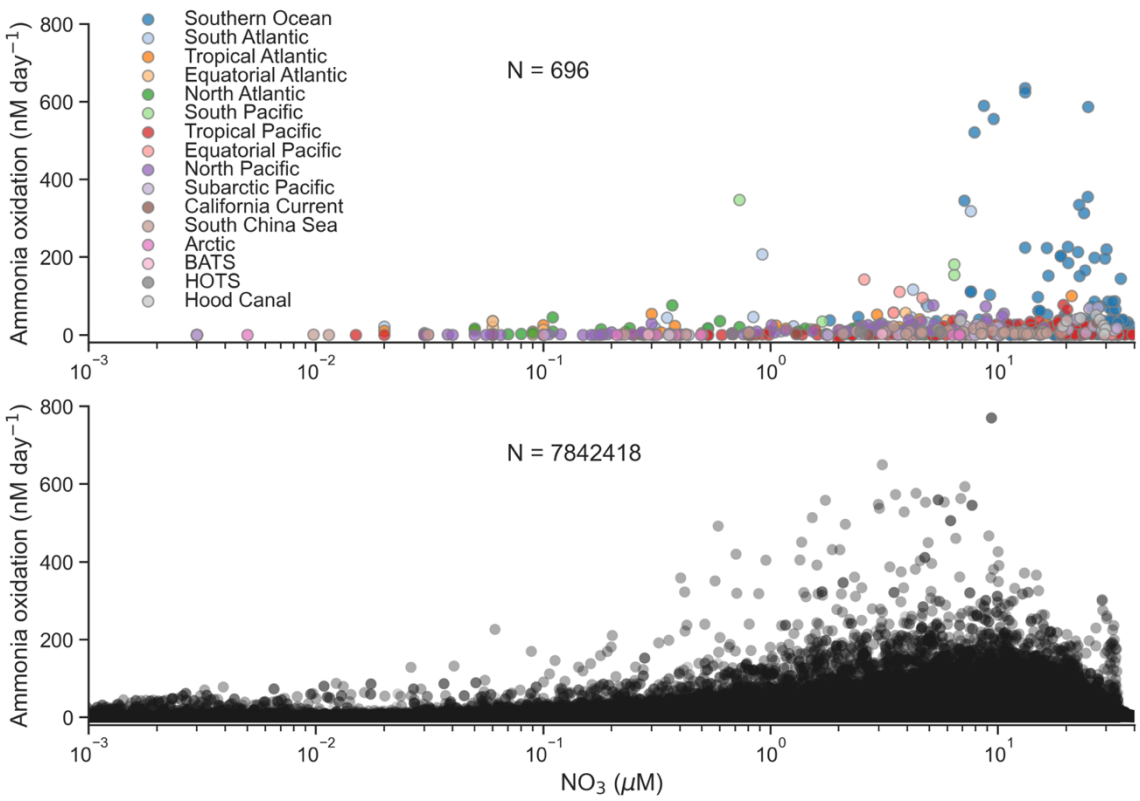

Figure S3. Measured (top) and modelled (bottom) ammonia oxidation rates from the global ocean plotted against the $\log_{10}$ of nitrate (NO_3), which indicates a spectrum of oligotrophy-eutrophy from left to right along the x-axis.

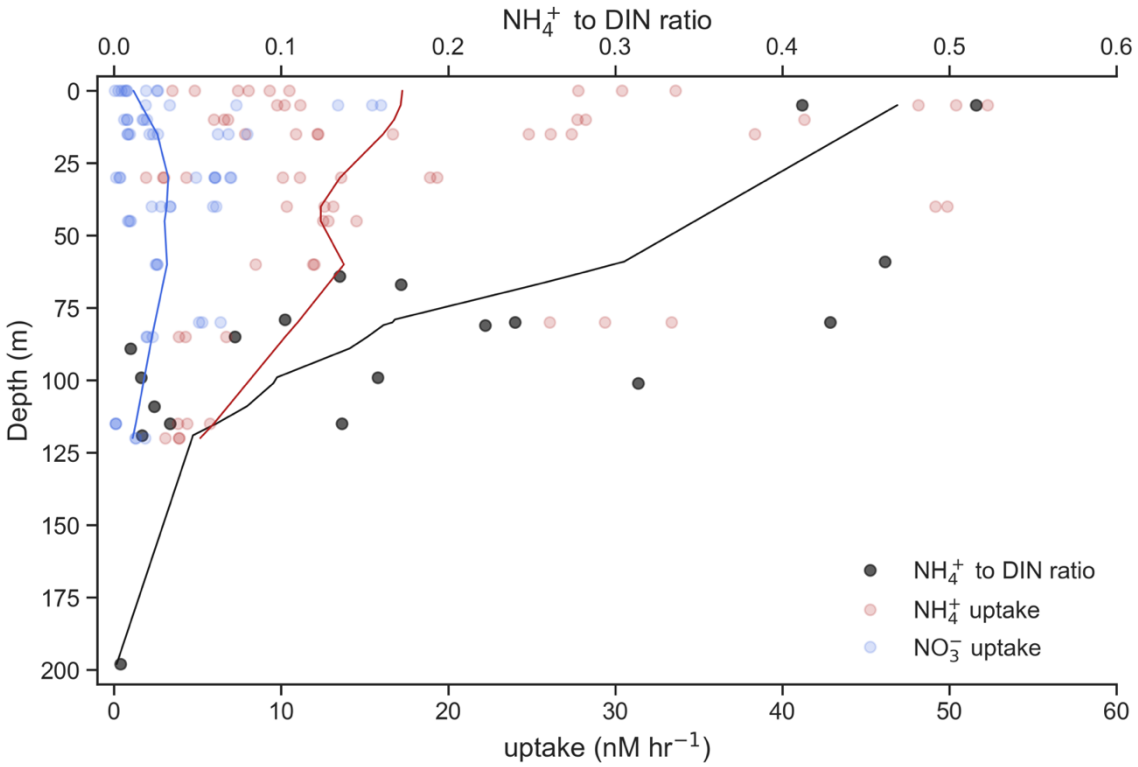

Figure S4. Nutrient and community uptake rate data from the Gulf of Mexico (Yingling et al., 2021). Linear interpolations in depth are constructed and the interpolated values are used in Figure S6.

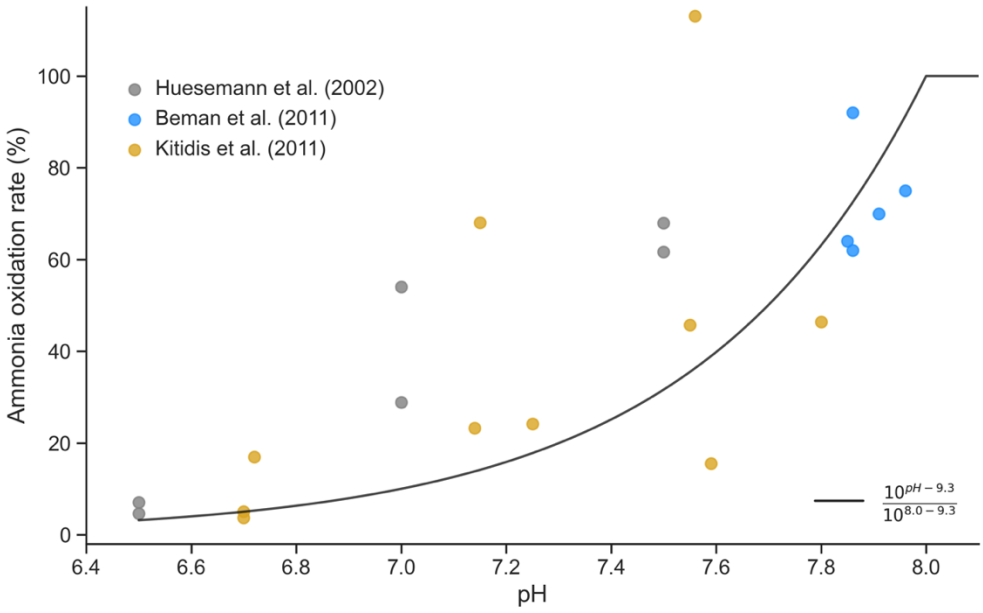

Figure S5. Parameterisation of ocean acidification on ammonia oxidation. Measurements of rate change in ammonia oxidation due to forced declines in pH (markers) are compared with a parameterisation for the relationship between pH and ammonia oxidation rate (solid line). This parameterisation returns a Pearson's correlation of 0.68 ($R^2 = 0.46$).

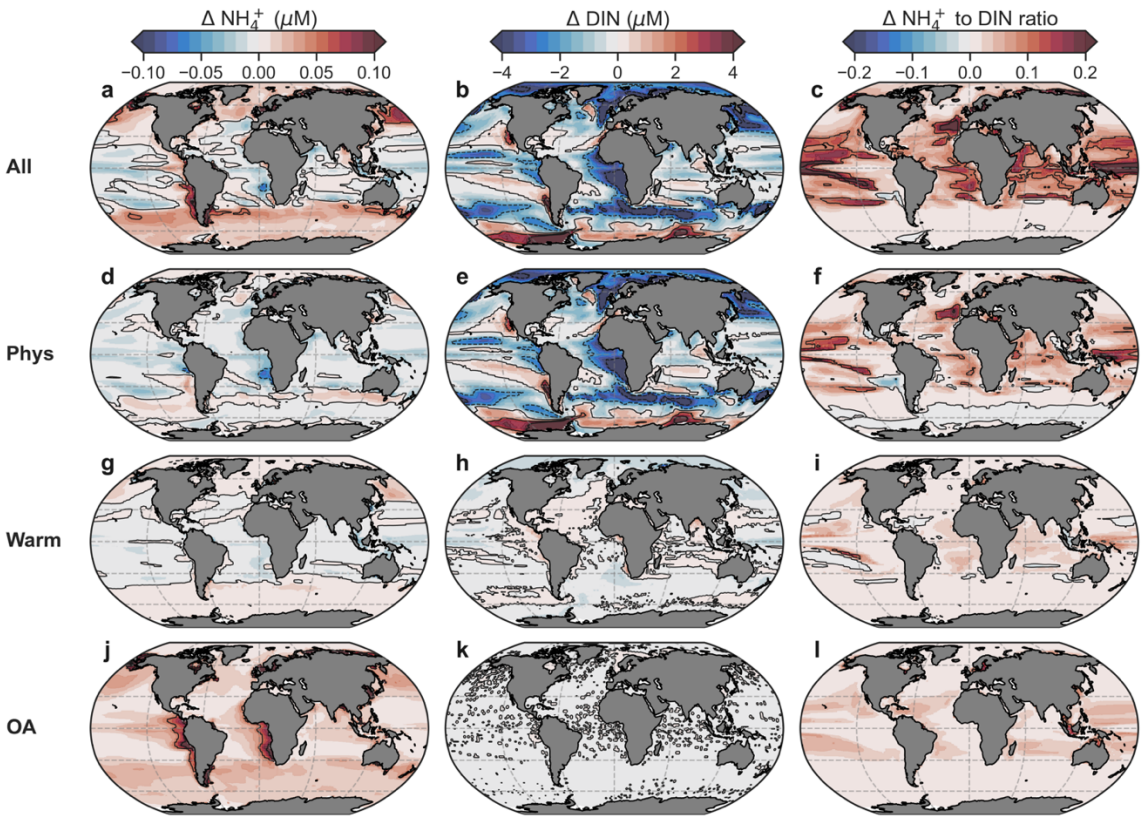

Figure S6. Anthropogenic impacts on concentrations of NH_4^+, DIN and NH_4^+:DIN ratios. a-c, The difference in concentrations and the NH_4^+ to DIN ratio averaged over the euphotic zone at the end of the 21st century (2081-2100) with all anthropogenic impacts (All). d-f, same as a-c but for physical changes (circulation + light) only (Phys). g-i, same as a-c but for warming effects on metabolism only (Warm). j-l, same as a-c but for ocean acidification only (OA).

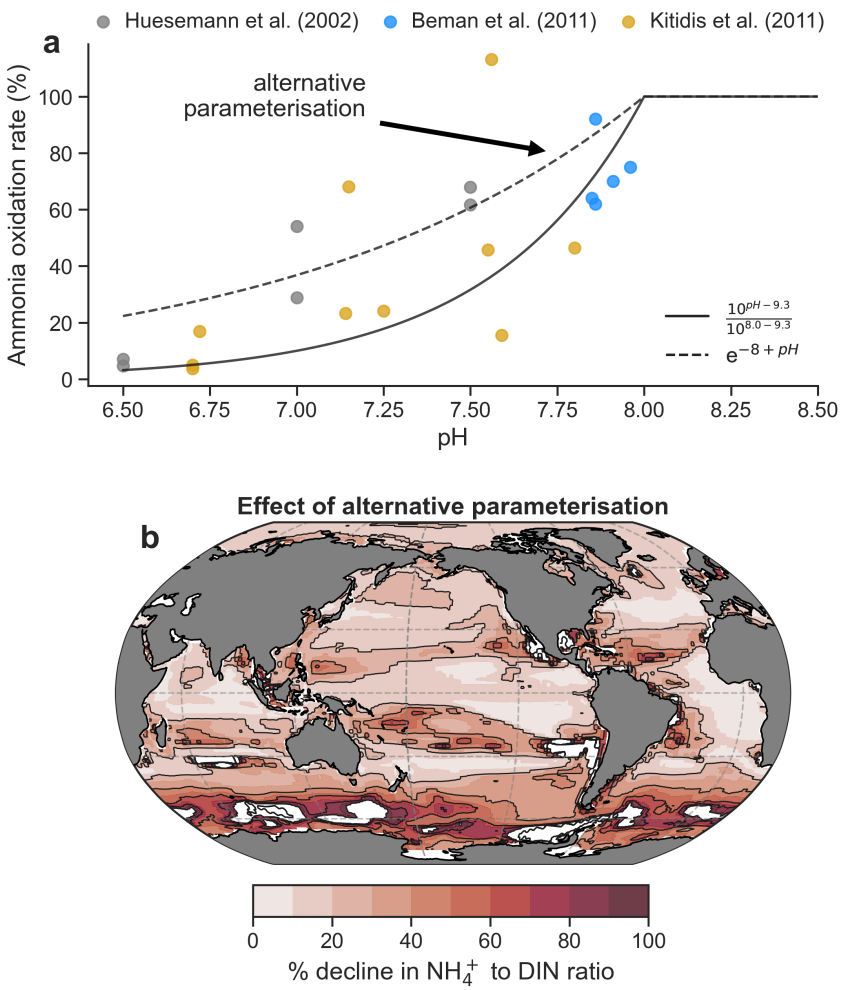

Figure S7. Alternative parameterisation of pH effect on ammonia oxidation. a, The alternative parameterisation (dashed line), which includes a weaker effect of pH decline on ammonia oxidation. b, How the weaker relationship between pH and ammonia oxidation ameliorates the increases in NH_4^+:DIN. As NH_4^+:DIN increases almost everywhere in these experiments, we only show how this alternative parameterisation works to reduce the increase.

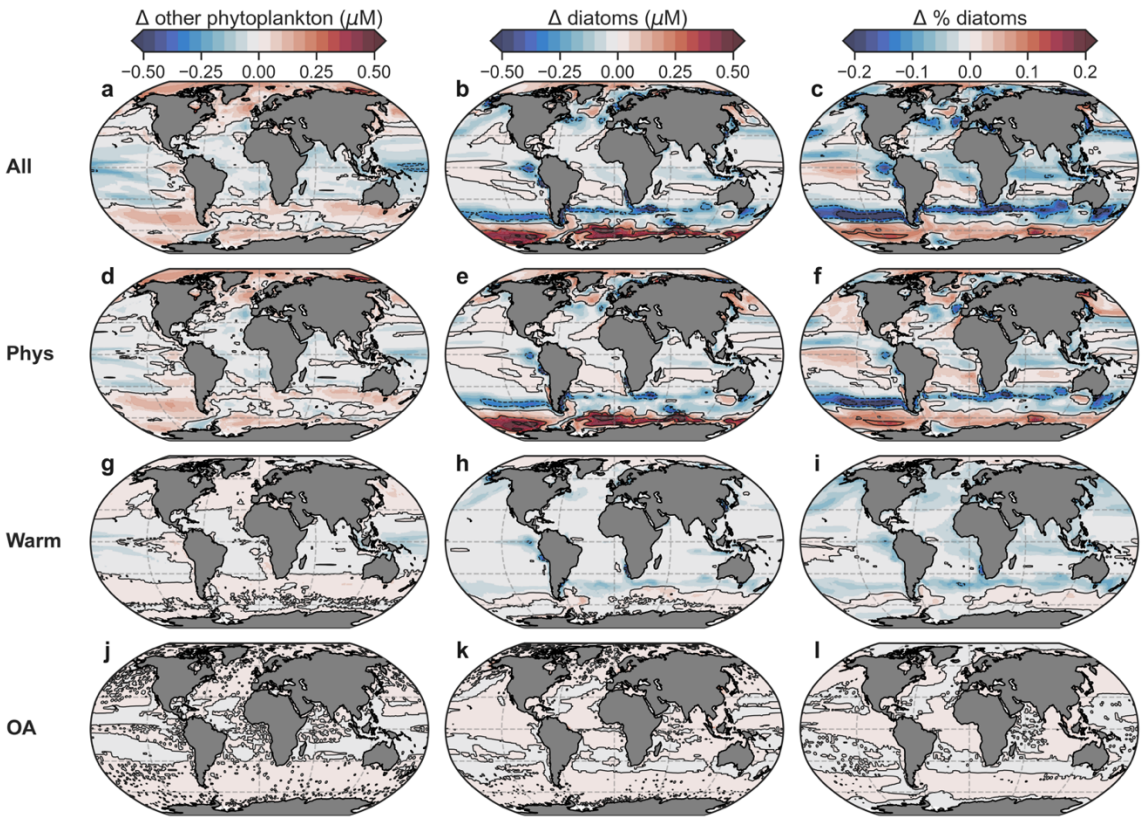

Figure S8. Anthropogenic impacts on concentrations of other phytoplankton, diatoms and the relative abundance of diatoms. a-c, Concentrations and the relative abundance of diatoms are averaged over the depths at which total phytoplankton concentrations are greater than 0.1 μM of carbon at the end of the 21st century (2081-2100) with all anthropogenic impacts (All). d-f, same as a-c but for physical changes (circulation + light) only (Circ). g-i, same as a-c but for warming effects on metabolism only (Warm). j-l, same as a-c but for ocean acidification only (OA).

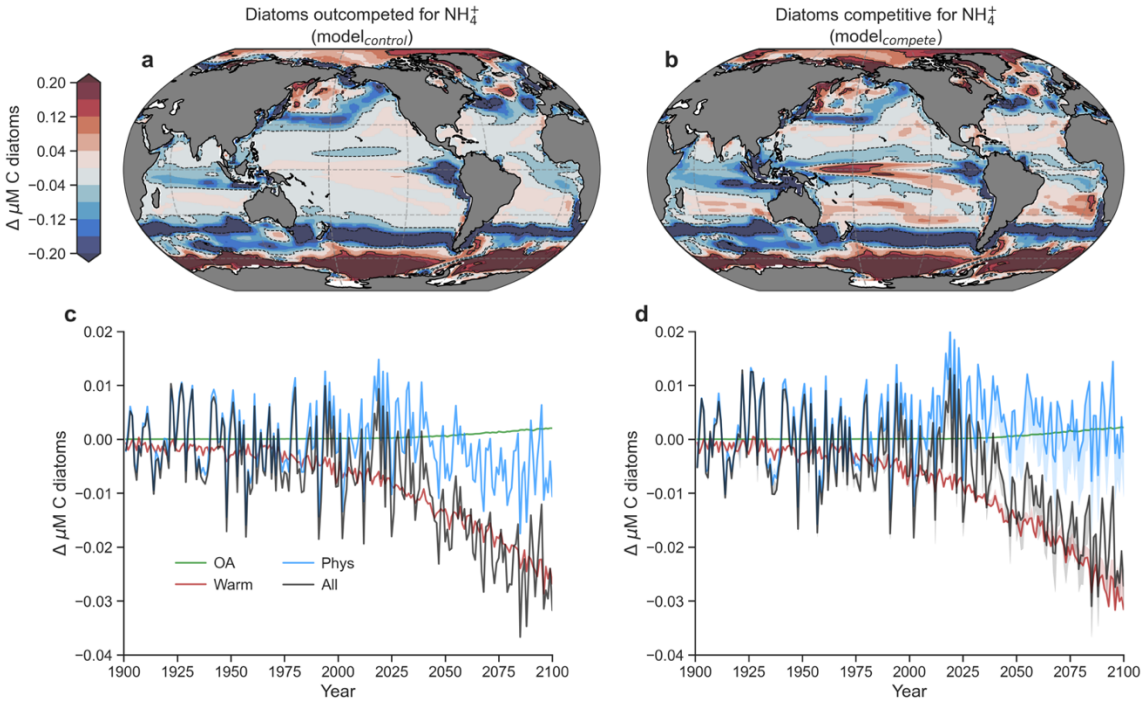

Figure S9. Impact of NH_4^+ enrichment within DIN on diatom abundance. (a), Mean change (Δ) in the abundance of diatoms (μM C) by the end of the 21st century (2081-2100) as predicted by the control run of the ocean-biogeochemical model (model$_{control}$) under the RCP8.5 scenario and averaged over the euphotic zone. (b), Same as in (a), but for the model with equal affinities of diatoms and other phytoplankton for NH_4^+ (model$_{compete}$). (c), Global mean change in diatom abundance due to physical (circulation + light) changes (blue), warming effects on metabolic rates (red), ocean acidification effect on ammonia oxidation (green) and all stressors (black) for model$_{control}$. (d), The same as in (c), but for model$_{compete}$. Shading shows the change between (c) and (d).

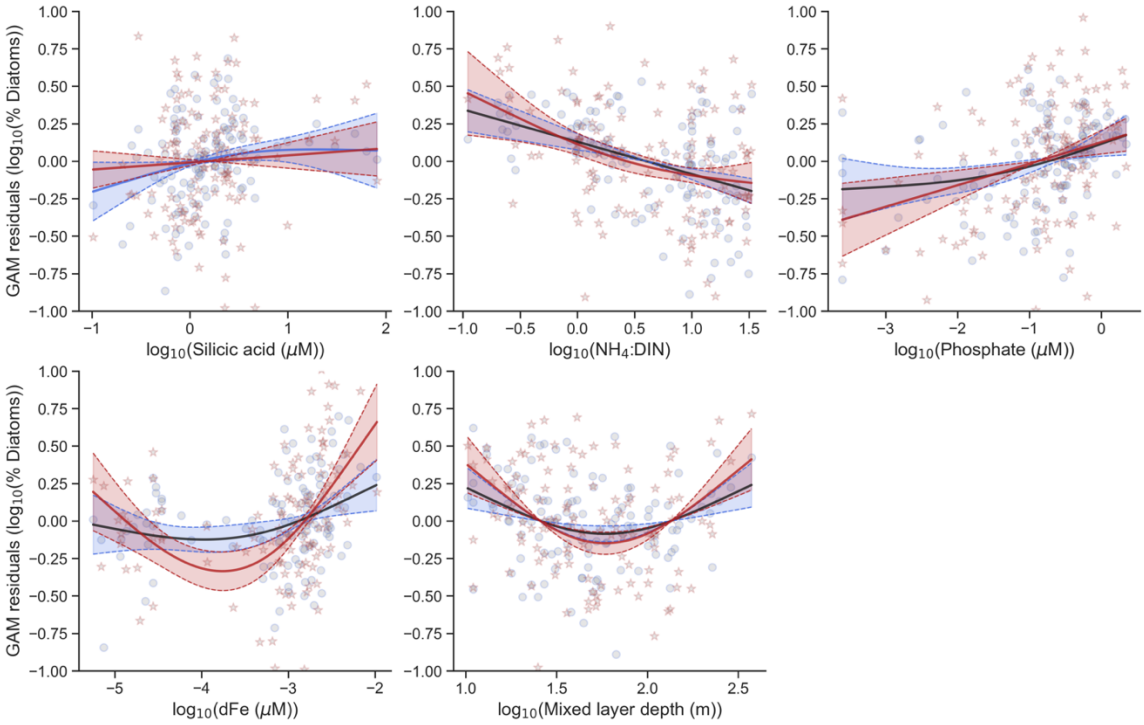

Figure S10. Key predictors of diatom relative abundance as a proportion of eukaryotic phytoplankton (blue) and all phytoplankton (red) generated by a GAM. The predictors are the $\log_{10}$ transformed silicic acid concentration (*in situ*), ratio of NH_4^+:DIN (model-derived), phosphate concentration (*in situ*), dissolved iron concentration (model-derived) and mixed layer depth (*in situ*). Dots are the partial residuals of the fitted GAM. The deviance explained and significance of each predictor are reported in Table S1.

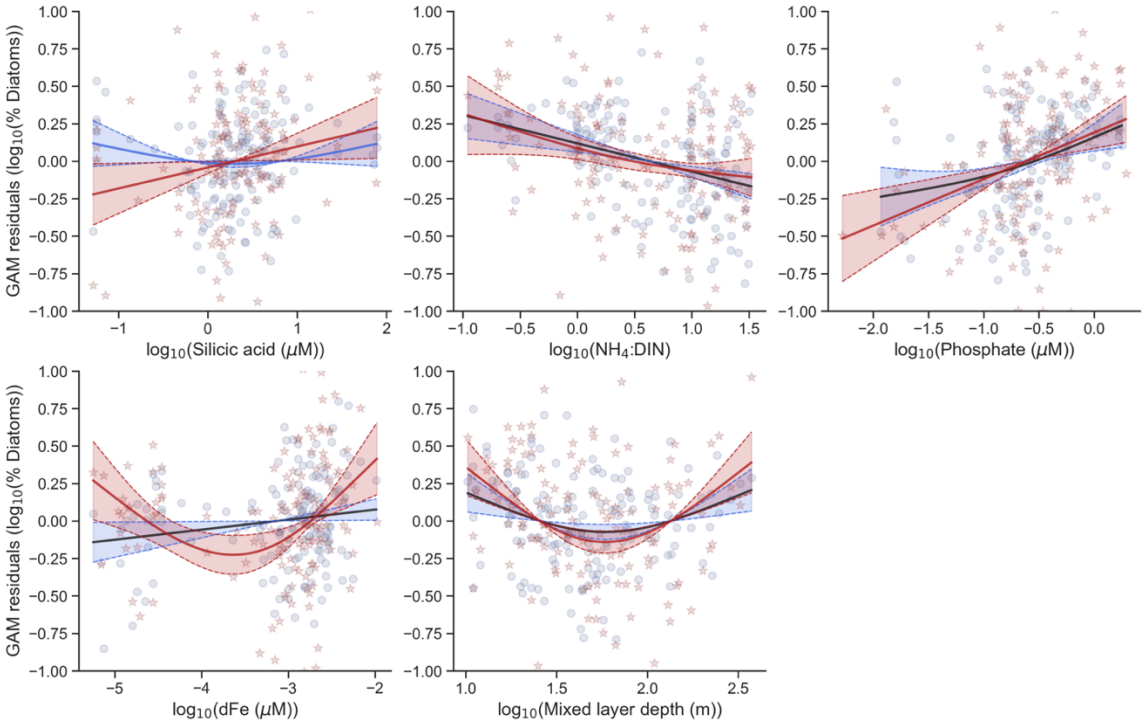

Figure S11. Key predictors of diatom relative abundance as a proportion of eukaryotic phytoplankton (blue) and all phytoplankton (red) generated by a GAM. The predictors are the $\log_{10}$ transformed silicic acid concentration (WOA18 (Garcia et al., 2019)), ratio of NH_4^+:DIN (model-derived), phosphate concentration (WOA18 (Garcia et al., 2019)), dissolved iron concentration (model-derived) and mixed layer depth (*in situ*). Dots are the partial residuals of the fitted GAM. The deviance explained and significance of each predictor are reported in Table S1.

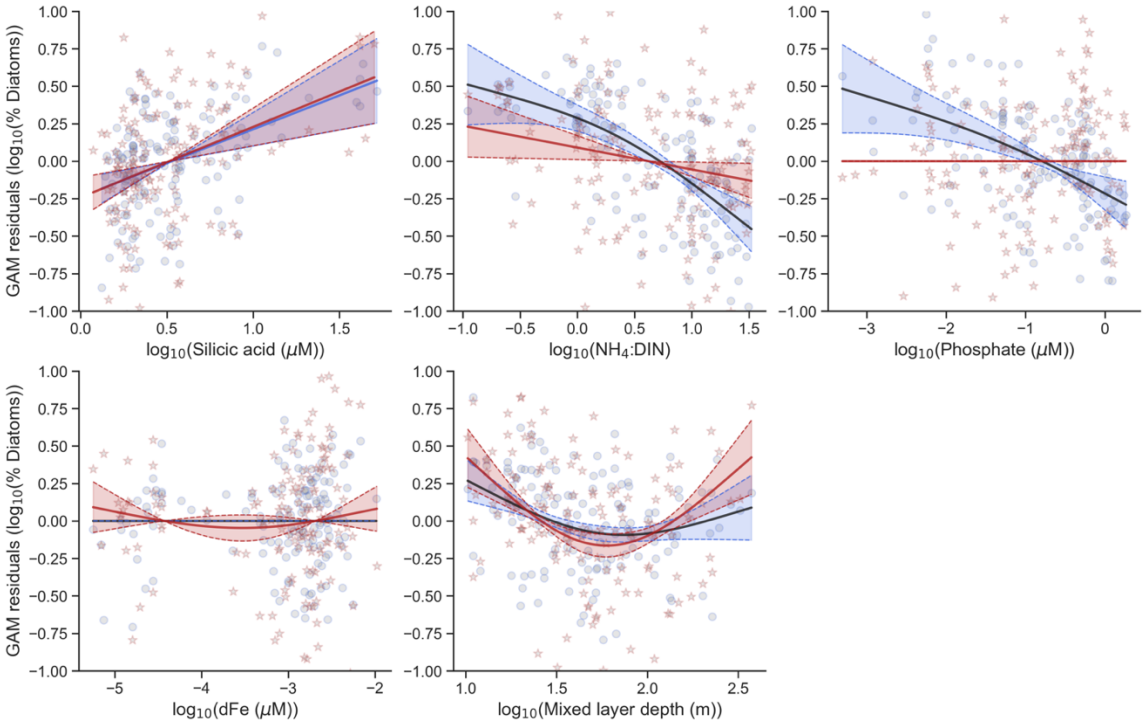

Figure S12. Key predictors of diatom relative abundance as a proportion of eukaryotic phytoplankton (blue) and all phytoplankton (red) generated by a GAM. The predictors are the $\log_{10}$ transformed silicic acid concentration (model-derived), ratio of NH_4^+:DIN (model-derived), phosphate concentration (model-derived), dissolved iron concentration (model-derived) and mixed layer depth (*in situ*). Dots are the partial residuals of the fitted GAM. The deviance explained and significance of each predictor are reported in Table S1.

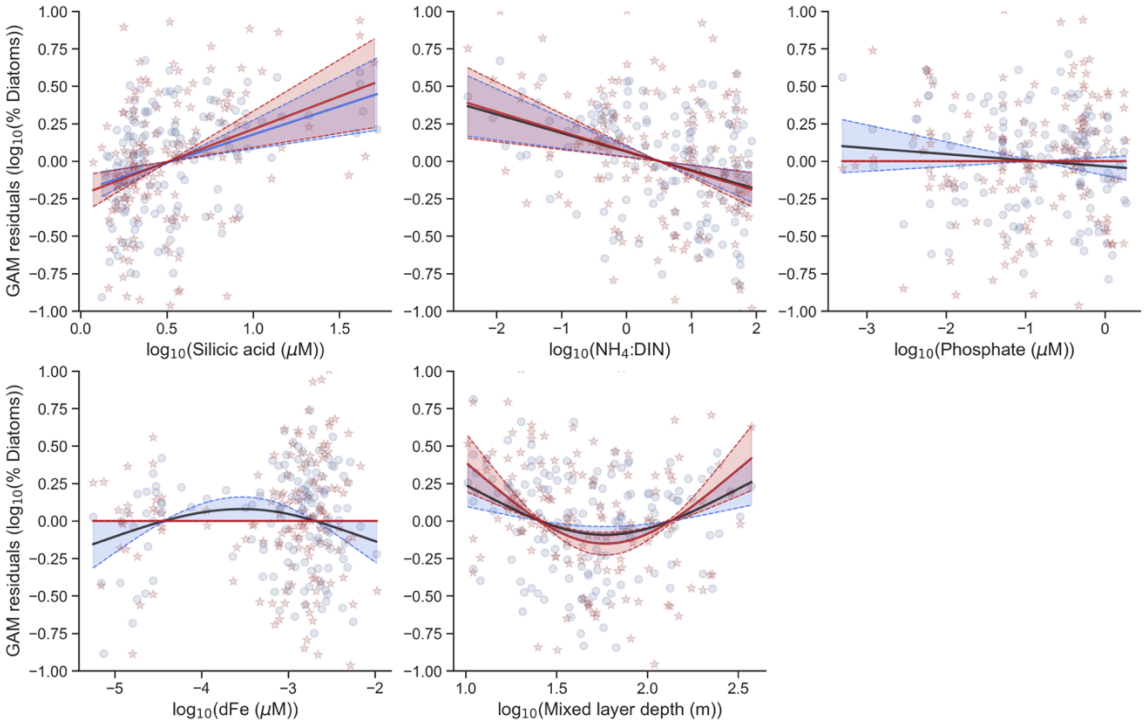

Figure S13. Key predictors of diatom relative abundance as a proportion of eukaryotic phytoplankton (blue) and all phytoplankton (red) generated by a GAM. The predictors are the $\log_{10}$ transformed silicic acid concentration (model-derived), ratio of NH_4^+:DIN (Darwin model), phosphate concentration (model-derived), dissolved iron concentration (model-derived) and mixed layer depth (*in situ*). Dots are the partial residuals of the fitted GAM. The deviance explained and significance of each predictor are reported in Table S1.

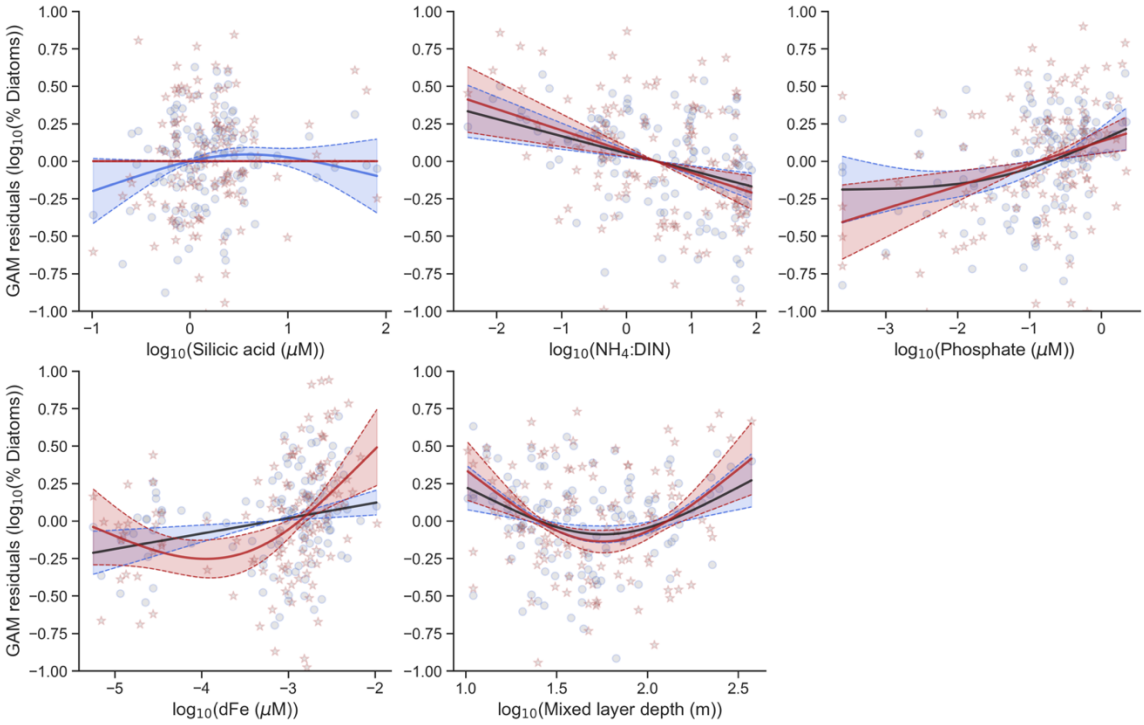

Figure S14. Key predictors of diatom relative abundance as a proportion of eukaryotic phytoplankton (blue) and all phytoplankton (red) generated by a GAM. The predictors are the $\log_{10}$ transformed silicic acid concentration (*in situ*), ratio of NH_4^+:DIN (Darwin model), phosphate concentration (*in situ*), dissolved iron concentration (model-derived) and mixed layer depth (*in situ*). Dots are the partial residuals of the fitted GAM. The deviance explained and significance of each predictor are reported in Table S1.

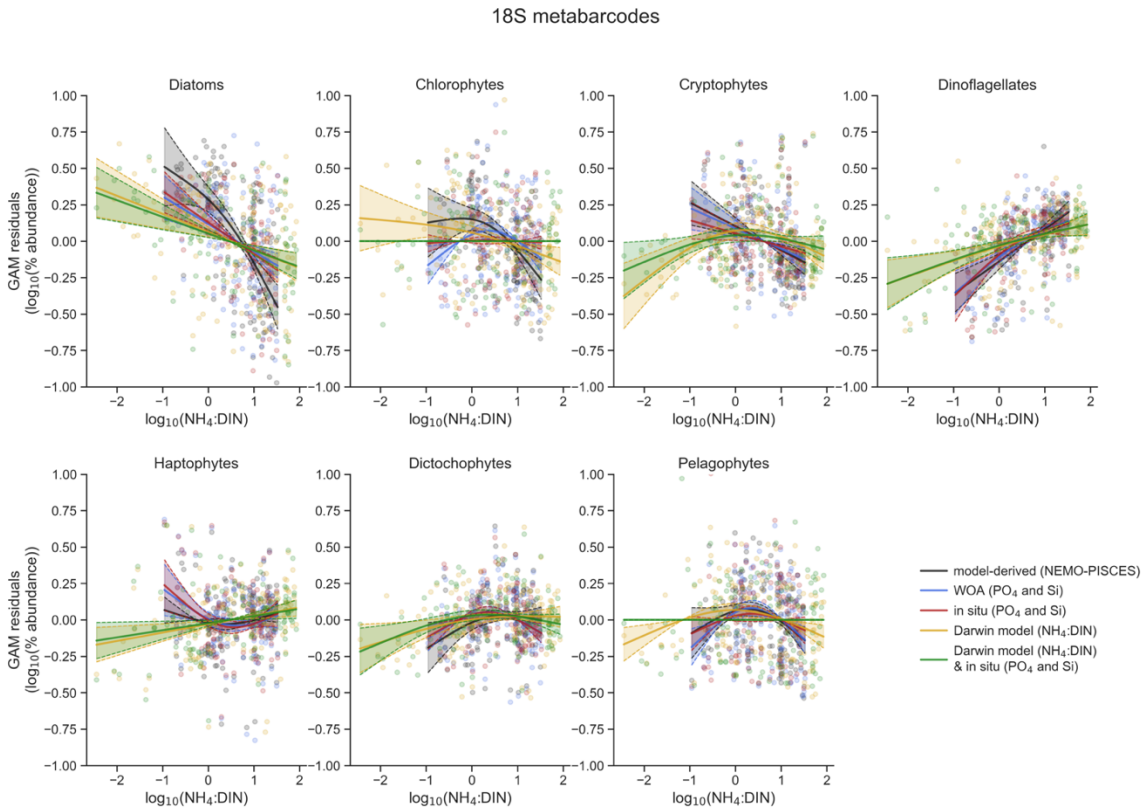

Figure S15. GAM relationships between NH_4^+ to DIN ratios and the relative abundance of each major phytoplankton taxa from the 18S metabarcoding estimates. Dots are the partial residuals of the fitted GAM. Each colour indicates a different combination of predictor variables.

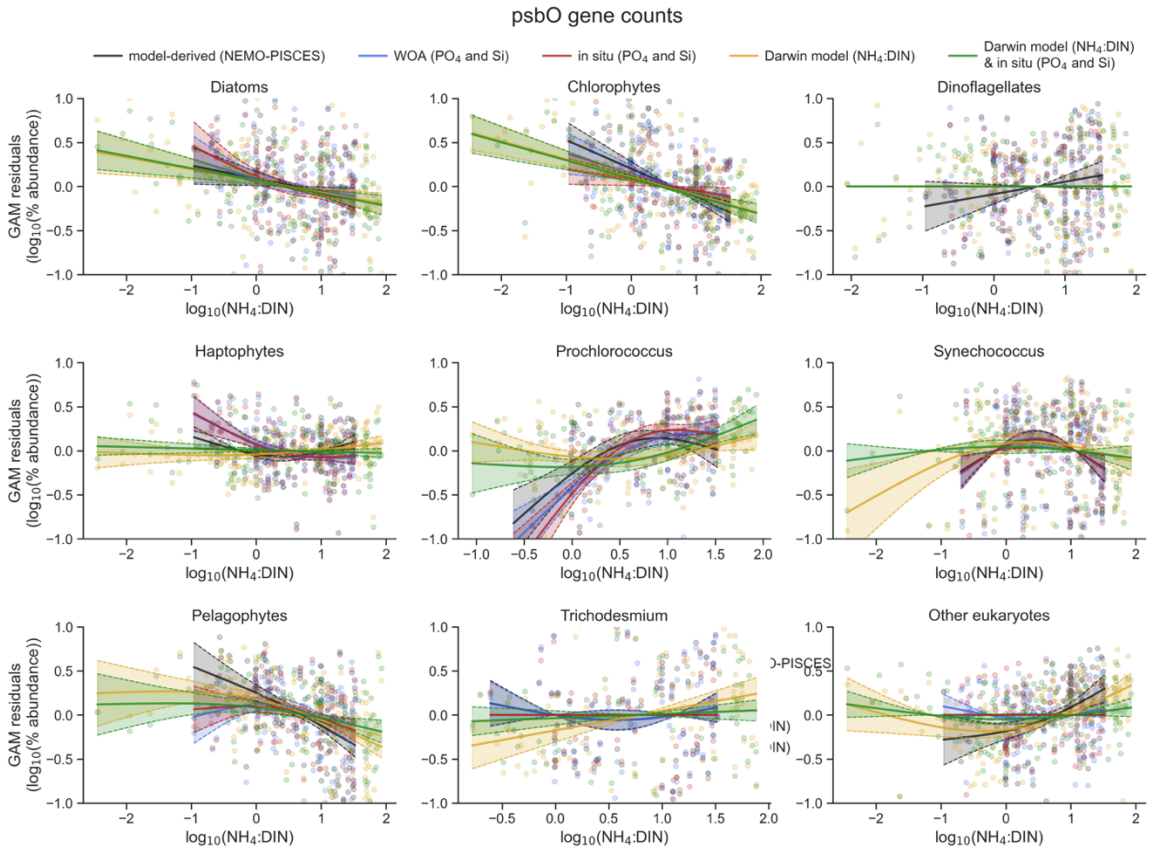

Figure S16. GAM relationships between NH_4^+ to DIN ratios and the relative abundance of each major phytoplankton taxa from the *psbO* gene count estimates. Dots are the partial residuals of the fitted GAM. Each colour indicates a different combination of predictor variables.

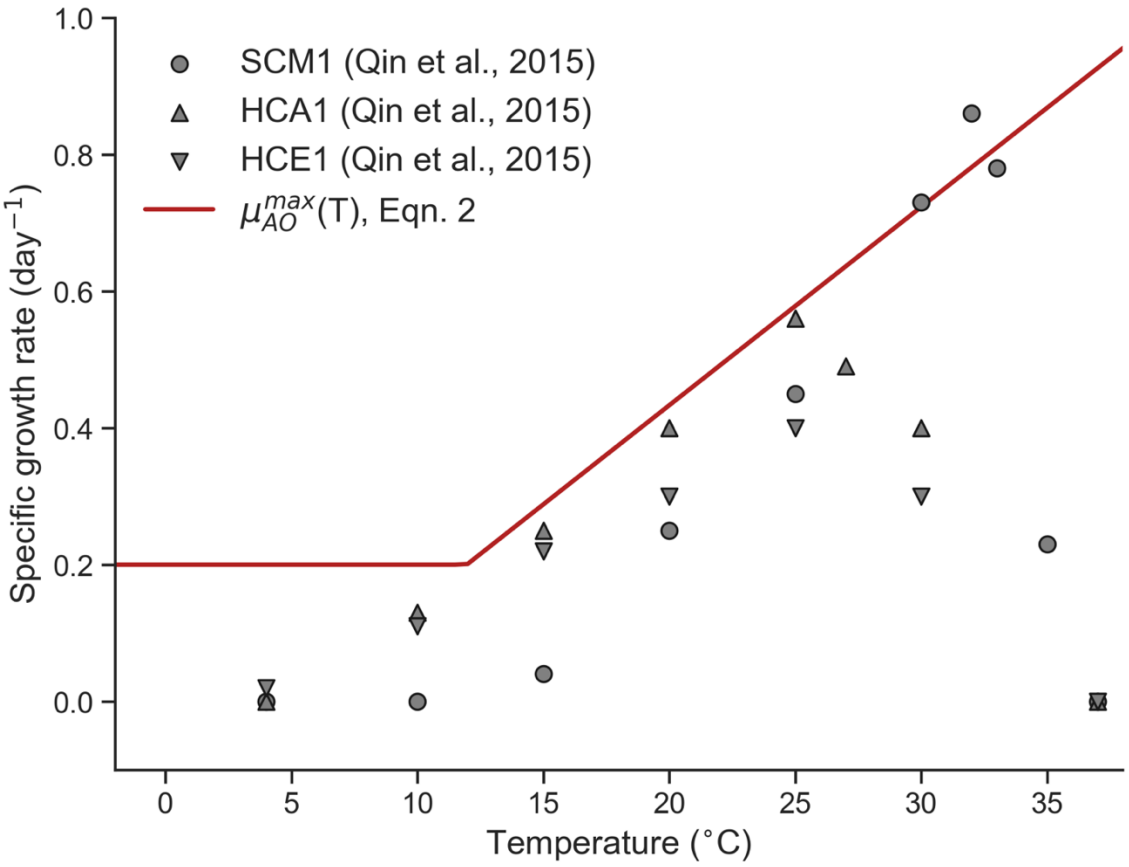

Figure S17. Temperature dependence of the maximum growth rate (μ) of ammonia oxidising archaea ecotypes (Qin et al., 2015).

significance	18S metabarcodes				
Predictor	**Model-derived**	**WOA**	***in situ***	**Darwin NH_4^+:DIN**	**Darwin + *in situ***
Si	***	ns	*	**	ns
NH_4^+:DIN	***	***	***	***	***
PO_4^{2-}	***	*	*	ns	**
dFe	ns	ns	*	ns	**
MLD	***	*	**	**	**
significance	***psbO* gene counts**				
Predictor	**Model-derived**	**WOA**	***in situ***	**Darwin NH_4^+:DIN**	**Darwin + *in situ***
Si	**	ns	ns	**	ns
NH_4^+:DIN	**	*	**	***	***
PO_4^{2-}	ns	**	**	ns	**
dFe	ns	**	***	ns	***
MLD	***	**	***	***	**
% Deviance explained	**18S metabarcodes**				
Predictor	**Model-derived**	**WOA**	***in situ***	**Darwin NH_4^+:DIN**	**Darwin + *in situ***
Si	24 (5)	21 (1)	17 (2)	24 (4)	17 (2)
NH_4^+:DIN	30 (16)	30 (4)	29 (7)	22 (6)	24 (2)
PO_4^{2-}	11 (8)	32 (3)	24 (3)	11 (1)	24 (4)
dFe	4 (0)	4 (1)	5 (5)	4 (2)	5 (4)
MLD	17 (6)	17 (3)	19 (5)	18 (5)	19 (5)
% Deviance explained	***psbO* gene counts**				
Predictor	**Model-derived**	**WOA**	***in situ***	**Darwin NH_4^+:DIN**	**Darwin + *in situ***
Si	25 (1)	17 (1)	13 (0)	25 (2)	13 (0)
NH_4^+:DIN	18 (2)	18 (2)	18 (3)	24 (4)	30 (3)
PO_4^{2-}	15 (0)	27 (4)	15 (4)	15 (0)	15 (3)
dFe	7 (1)	7 (6)	13 (13)	7 (0)	13 (8)
MLD	19 (9)	19 (5)	21 (7)	19 (6)	21 (6)

Table S1. Generalized Additive Model (GAM) results for predictions of the relative abundance of diatoms. Data provided by *Tara* Oceans 18S rRNA gene metabarcoding and *psbO* gene counts. Rows are the different predictor variables. Si = Silicate, PO_4^{2-} = Phosphate, dFe = dissolved iron, MLD = mixed layer depth. Significance is assessed by applying a smoothing penalty to the predictor in question. Deviance explained is calculated by fitting a GAM with only the predictor in question, and by removing the predictor from the full model and comparing the difference in deviance explained with the full model (this result is provided in the parantheses). The most significant or most

explanatory are highlighted. (*) p-value < 0.05. (**) p-value < 0.01. (***) p-value < 0.001.

18S metabarcodes		
Taxa	**Model-derived**	**Darwin model**
Diatoms	29.9% (***)	21.6% (***)
Cryptophytes	2.4%	4.3% (*)
Chlorophytes	2.6%	1.6%
Dinoflagellates	36.8% (***)	30.6% (***)
Haptophytes	4.3% (*)	5.9% (**)
Dictyochophytes	9.1% (**)	11.4% (***)
Pelagophytes	0.0%	6.8% (**)
***psbO* gene counts**		
Taxa	**Model-derived**	**Darwin model**
Diatoms	17.6 (***)	24.3% (***)
Prochlorococcus	23.4% (***)	16.0% (***)
Synechococcus	5.9% (**)	7.7% (**)
Chlorophytes	13.2% (***)	21.2% (***)
Dinoflagellates	1%	0.0%
Haptophytes	13.6% (***)	1.2%
Pelagophytes	11.2% (***)	12.5% (***)
Trichodesmium	4%	9.3% (**)
Other eukaryotes	0.1%	8.5% (**)

Table S2. Deviance explained from the Generalized Additive Models using NH_4^+:DIN as the sole predictor of the relative abundance of different eukaryotic phytoplankton taxa. Data provided by *Tara* Oceans 18S rRNA gene metabarcoding and *psbO* gene counts. Significance of NH_4^+:DIN as a predictor of diatom relative abundance is denoted by the number of *. No * means p-value > 0.05. (*) p-value < 0.05. (**) p-value < 0.01. (***) p-value < 0.001. NH_4^+:DIN may be model-derived from PISCES-v2 or from the Darwin model (Follows et al., 2007).

Parameter	Description	Value	Units
μ_{AO}^{max}	Maximum rate of ammonia oxidation	Eqn. 2	day^{-1}
$K_{AO}^{NH_4^+}$	Ammonia oxidation half-saturation constant for ammonium	0.1	$mmol\ m^{-3}$
K_{AO}^{PAR}	Ammonia oxidation half-saturation constant for photosynthetically active radiation	0.75	$W\ m^{-2}$
R_{AO}^{pH}	Reference pH below which ammonia oxidation is limited	8.0	pH units
pK_a	pH at which all NH_x is NH_3	9.3	pH units
μ_{NO}^{max}	Maximum rate of nitrite oxidation	0.15	day^{-1}
$K_{NO}^{NO_2^-}$	Nitrite oxidation half-saturation constant for nitrite	0.1	$\mu mol\ m^{-3}$
K_{NO}^{PAR}	Nitrite oxidation half-saturation constant for photosynthetically active radiation	0.75	$W\ m^{-2}$

Table S3. Parameters and their values used to simulate ammonia and nitrite oxidation in the PISCES-v2 ocean biogeochemical model, detailed in equations 1-8. Values are informed by field and laboratory studies cited in the methods.

Data Set S1. Nutrient concentration data.

Data Set S2. Ammonia oxidation rate data.

Data Set S3. Coincident nutrient and regenerated to new primary production rate data.

Data Set S4. Variations in ammonia oxidation rates for pH changes. Rates normalized to a pH of 8.